EULER-BERNOULLI IMPLEMENTATION OF SPHERICAL ANEMOMETERS FOR HIGH WIND SPEED CALCULATIONS VIA STRAIN GAUGES

A Thesis

by

DAVIS MATTHEW CASTILLO

Submitted to the Office of Graduate Studies of
Texas A&M University
in partial fulfillment of the requirements for the degree of

MASTER OF SCIENCE

May 2011

Major Subject: Aerospace Engineering

Euler-Bernoulli Implementation of Spherical Anemometers for High Wind Speed Calculations via Strain Gauges

EULER-BERNOULLI IMPLEMENTATION OF SPHERICAL ANEMOMETERS FOR HIGH WIND SPEED CALCULATIONS VIA STRAIN GAUGES

A Thesis

by

DAVIS MATTHEW CASTILLO

Submitted to the Office of Graduate Studies of
Texas A&M University
in partial fulfillment of the requirements for the degree of

MASTER OF SCIENCE

Approved by:

Chair of Committee,	John E. Hurtado
Committee Members,	Shankar Bhattacharyya
	Edward B. White
Head of Department,	Demitris Lagoudas

May 2011

Major Subject: Aerospace Engineering

ABSTRACT

Euler-Bernoulli Implementation of Spherical Anemometers for High Wind Speed Calculations via Strain Gauges. (May 2011)

Davis Matthew Castillo, B.S., Southern Methodist University

Chair of Advisory Committee: Dr. John E. Hurtado

New measuring methods continue to be developed in the field of wind anemometry for various environments subject to low-speed and high-speed flows, turbulent-present flows, and ideal and non-ideal flows. As a result, anemometry has taken different avenues for these environments from the traditional cup model to sonar, hot-wire, and recent developments with sphere anemometers. Several measurement methods have modeled the air drag force as a quadratic function of the corresponding wind speed. Furthermore, by incorporating non-drag fluid forces in addition to the main drag force, a dynamic set of equations of motion for the deflection and strain of a spherical anemometer's beam can be derived. By utilizing the equations of motion to develop a direct relationship to a measurable parameter, such as strain, an approximation for wind speed based on a measurement is available. These ODE's for the strain model can then be used to relate directly the fluid speed (wind) to the strain along the beam's length.

The spherical anemometer introduced by the German researcher Holling presents the opportunity to incorporate the theoretical cantilevered Euler-Bernoulli beam with a

spherical mass tip to develop a deflection and wind relationship driven by cross-area of the spherical mass and constriction of the shaft or the beam's bending properties.

The application of Hamilton's principle and separation of variables to the Lagrangian Mechanics of an Euler-Bernoulli beam results in the equations of motion for the deflection of the beam as a second order partial differential equation (PDE). The boundary conditions of our beam's motion are influenced by the applied fluid forces of a relative drag force and the added mass and buoyancy of the sphere. Strain gauges will provide measurements in a practical but non-intrusive method and thus the concept of a measuring strain gauge is simulated. Young's Modulus creates a relationship between deflection and strain of an Euler-Bernoulli system and thus a strain and wind relation can be modeled as an ODE.

This theoretical sphere anemometer's second order ODE allows for analysis of the linear and non-linear accuracies of the motion of this dynamic system at conventional high speed conditions.

DEDICATION

To my greatest inspirations,

My wife and best friend, Samantha,

My dear parents, Luis and Maria,

And My Lord up above.

ACKNOWLEDGEMENTS

First, I would like to thank my advisor, Dr. John E. Hurtado. His support these past few years has meant everything to my career. His advice and encouragement have helped me understand concepts and theories that at times appeared to be of a foreign language. His patience has not only helped with research but with the struggles of everyday life. I look forward to using his sound advice now and well into my career.

I would like to thank my committee members, Dr. Shankar Bhattacharyya, and Dr. Edward White, for their support of my research. Dr. Bhattacharyya your classes in controls helped challenge me to a better understanding of control theory. I would especially like to thank Dr. Othon Rediniotis for his help in understanding some basic concepts of fluid theory, which helped my research immensely. A special thanks to Dr. Haisler and Karen Knabe for helping me get through the administrative hurdles which I found myself having to jump over frequently.

I would like to acknowledge the financial support of the Human Diversity Fellowship and the Aerospace Department. I am also thankful for the research work with Kane's Method at NASA JSC with L-3 colleagues Dan Erdberg and Dr. Tushar Gosh.

During my graduate years at Texas A&M University, I give thanks to the inspiration and support from those closest, including, but not limited to Bryan Castillo, Roberto Espinosa, Ruby Rodriguez, Juan Enciso, Ian Horbaczewski, Amanda Oleksy, Martin Ore, and Sharon Morgan. Whether in need for words of wisdom, a friend to study, a workout partner, or help with tough times you have been there for me.

Thanks to my wife for her numerous sacrifices the past few years. Her motivation and encouragement have helped me become a better man. Also, thanks to my wife for the many times she helped edit and review my thesis. Finally, thanks to my parents for listening and offering support through the hardest of times. Thank you for believing in me and always being proud. Most importantly, however, thanks to my father in heaven for the strength and spirit to accomplish another life goal.

NOMENCLATURE

β, β_i	Frequency Coefficient and Harmonic of χ
c	Distance of Strain Gauge from Center of Beam
C_a	Added Mass Coefficient
C_D	Drag Coefficient
δ^K	Kroneker Delta Function
δ^D	Dirac Delta Function
δ	Variation Operator
$\hat{e}_r, \hat{e}_\theta, \hat{e}_\varphi$	Spherical Coordinate Unit Vectors
$\varepsilon(x,t)$	Strain of Beam
$\hat{\varepsilon}$	Approximate Strain with Measurement Error
E	Young's Modulus
F_D	Drag Force from Wind
F_B	Buoyancy Force
F_{AM}	Added Mass Force
I	Second Moment of Inertia of Beam
LHS	Left Hand Side Notation
m_{sphere}	Mass of Sphere
ρ_b, ρ_f	Linear Density of Beam, Density of fluid
$\phi(x,t)$	Potential Fluid Function
R_S, R_b	Radius of Sphere, Beam

RHS	Right Hand Side Notation
$U, \dot{U}$	Wind Speed, Wind Acceleration
$\widehat{U}$	Estimated Wind Speed

TABLE OF CONTENTS

CHAPTER Page

LIST OF FIGURES

CHAPTER I

INTRODUCTION

This thesis will focus on the analytical modeling of a hybrid body in a high wind speed environment and the effect of the induced flow forces in a non-viscous fluid. Hybrid bodies have not always been used to describe bodies of mass in motion due to the extra degrees of freedom brought into the analytical calculations as a result. It is common practice to use rigid bodies in most dynamic calculations to avoid the nonlinearities that a multi-body system can encounter. Additionally, continuous bodies can experience sheer stresses and compressions among an indiscrete domain; thus, these additional nonlinearities will impose a variable force in the multi-body system equation of motion.

Classical Mechanics is often applied to rigid bodies to model their equations of motion. These simple systems have the center of mass as the object of interest for the body's motion. Aerodynamics however requires precision for every degree of freedom in the system; consequently, external forces applying sheer stress and compression to a continuous body are subject to numerous influences per point. Finite element methods have been used often to deal with the additional degrees of freedom that these complex bodies of masses entail. However, for our theoretical problem we will approach our modeling of the continuous body with generalized coordinates. In this thesis we will use Lagrange's equations for the continuous beam and rigid sphere mass proposed for the

---

The journal model is IEEE *Transactions on Automatic Control.*

anemometer system.

Current research focused on anemometry has made breakthroughs in new measurement techniques suited for specific conditions [1]. The hybrid model used by Holling, via optics, a spherical anemometer is used to calculate highly oscillating wind speeds to a greater capacity than the traditional cup anemometer design and to a similar accuracy as that of the hot wire anemometer [2]. As a result this spherical anemometer is calibrated to react with the given wind environment and then extrapolated for a differential model.

With the increase of natural disasters, wind environments can take many forms. Tornadoes and high wind speeds of nature can be catastrophic. Careful analysis by a record of wind speeds in particular neighborhoods could provide benefits to insurance companies, meteorology, and even civilians. For this reason a robust method of providing an anemometer to provide accurate but inexpensive readings could be a tool to be used in the future. Because wind forces can act in unpredictable ways and wind anemometer with recording abilities could help determine the wind speeds experiences at one home versus another within close vicinity.

This experimental model has contributed an innovative way to absorb these contributing forces and relating the wind speed based on the beam's deflection. The experimental work established has as a result brought motivation to develop a full dynamical analysis of this hybrid model to create the equations of motion for a spherical anemometer including additional inline fluid forces that may not be included in traditional approximations.

The nonlinearities consist of the concepts of the added mass phenomenon, buoyancy, and drag forces. Although these wind forces can prove to be minimal in most low fluid density environments, the dynamical model will prove significance, or lack thereof, in such a system. The goal of the integration of these fluid influences into this theoretical model is a robust second order differential system which can output wind measurement approximations for a given wind model.

Creating this robust dynamical model will require accuracy in the calculation of the deflection in an experimental setting. The development of an estimated dynamic model for the wind speed according to the equations of motion will be achieved by adopting this comprehensive model. The basis for this theory's development consists of the theories of separation of variables, Euler- Bernoulli beams, Hamilton's Principle, Lagrange's Equations, and steady state solutions.

The development of these necessary theories will construct the dynamic model to estimate the wind speed of the given experimental environment. By simulating the dynamic ODE model for the motion of the spherical anemometer, the system's response to varying beam properties and wind conditions can be further analyzed. The steps taken to achieve this dynamic model are as follows:

1. Develop the distinct nonlinear fluid forces which will affect this hybrid system.
2. Research the properties of continuous bodies for the beam of this spherical anemometer.

3. Use Hamilton's principle via Lagrange Method to conjure equations of motion for the hybrid system.
4. Incorporate the boundary conditions for the given system requirements to satisfy the beam and sphere's motion subject to all forces in system.
5. Develop a relationship between the beam's deflections via EOM into the corresponding wind speed.
6. Calculate the partial differential equations using separation of variables and uncoupling methods.
7. Create a relationship between strain and the differential equations of motion.
8. Test the dynamic model of strain for behavior.
9. Reiterate process with simulated measurement error to project strain and wind speed relationship.
10. Implement data recording method for complete simulation.

Once the methodology is achieved, the model will be applied for a variety of simulation test cases to verify the accuracy to given wind models.

CHAPTER II

BACKGROUND

This chapter will briefly introduce the different ways anemometers measure and approximate wind speed to assemble distinct and similar qualities to the spherical anemometer. A further description of the Newtonian physics of the fluid induced forces affecting the spherical anemometer's motion will be developed to bond the relationship between force and motion. For further investigation of the motion of this anemometer particularly, the beam, an assertion has to be made to define this beam as a continuous body which thus has infinite number of positions in motion. The development of kinematics of this hybrid body of mass will be aided by using Hamilton's Principle and Lagrange's Method.

The contributions by Holling and Blevins consist as the central ideas for this model. The concepts and derivations of the corresponding fluid forces for this model will be further explained by applying known fluid properties from works by Blevins. The deflection, motion from the neutral axis, calculated via Lagrange's Method will then become important in developing the relationship to the sought after wind speed approximation in the proceeding chapter.

A. Anemometer Background

The purpose of anemometers when they were first developed was simple; it needed to find a method to calculate practical wind speeds. The basic model consists of a

number of hemispherical cups connected in an array form by rods to a central vertical shaft. The use of the cup anemometer simply approximates the wind speed by the number of turns by the cups due to the wind force applied in a specific period of time. Hot-wire anemometers have also been used for high frequency analysis of rapidly changing winds found in turbulence wind conditions. Holling's experiment revealed a rapidly changing wind environment is best read with a hot-wire anemometer for speed; however, the sphere anemometer more frequently provides better approximations of the wind model's speed without over-speeding like the traditional cup anemometer does in the same environment. The sphere anemometer demonstrates an improvement from the over-speeding problem the cup anemometer showed with higher frequency winds [2].

B. Using Spherical Anemometer

Holling's model proves that the wind induces a drag force to be the main driving component of the beam's excitation and motion; for this case, the drag will be a component to develop and include in the beam model's equations. Blevins's contribution to buoyancy and added mass forces for flow induced models will contribute to the rest of the force application for this model. The flexibility of this anemometer contributes to the hybrid aspect of this body mass and thus introduces a different kinematic model with specific properties. The flexibility in this spherical anemometer can lead to several uncertainties and degrees of freedom as a result but for the purpose of the wind conditions and model needed we will assume the Euler Bernoulli Beam properties for the flexible vertical shaft of this anemometer.

C. Drag Forces

Drag has been used in a general basis as a force with quadratic velocity dependence,

$$F_D = \frac{1}{2}\rho_{fluid} v^2 A C_D \tag{2-1}$$

The drag force is best suited to comply at relative high fluid speeds (wind speed in this case). Ideal flow is assumed to avoid additional considerations such as shear, viscosity, and other fluid non-linearities. These generalizations are made with the consideration that the wind speed of the environment is much greater than the speed of the body mass. However, when considering fluids and masses that accelerate quickly, a beam with a relative drag force is better suited according to Blevins's formula [3].

$$F_{D_{lin}} = \frac{1}{2}\rho_{fluid}|U - \dot{y}|(U - \dot{y})DC_D \tag{2-2}$$

In this linear relative drag force $F_{D_{lin}}$ it be must be noted that the measured units are that of Newtons per length of the cross section. The rest of the variables are familiar to the traditional drag force such as a varying drag coefficient, C_D (dependent on the shape of the body mass) in the given fluid with density ρ_{fluid}. When given the scenario of the anemometer exposed to a wind environment governed as $U(t)$'s properties, the drag force is dynamically dependent upon the fluid speed, U, and the speed of the anemometer, $\dot{y}$. The motion of the anemometer, y references the deflection from the beam's neutral axis, position at complete rest. This beam's deflection, y, is both a function of time and position since the deflection of the beam will vary along the beam

and with respect to time. The numerous points of motion and deflection will make the drag force of the anemometer in its entirety complex due to the drag forces subject not just upon the spherical mass but also along the beam of the anemometer. However if a spherical mass's cross sectional area can be relatively large compared to a thin beam's cross sectional area; consequently, the drag along the thin beam can be neglected. The parameter considerations in Chapter 5 will detail the equations used to make the mentioned assumptions.

D. Buoyancy and Added Mass Concepts

Two additional forces that develop for a mass present in a fluid flow include buoyancy and added mass. Air is still subject to same inline fluid forces as denser fluids such as water but air's significantly lower density lowers the magnitude of these two forces.

Buoyancy is commonly referred to in examples masses submerged in fluids, commonly water, to show the fluid force phenomenon opposing other forces such as gravity. Added Mass is also present in the movements of mass structures submersed in fluids under fluid acceleration.

Both of these are considered inline forces and a result of the pressure gradient present at the surface of the mass subject to the wind speed model. This inertial force as described by Blevins can be calculated by means of the integral equation for

$$F_x = \oiint_S p \cdot \hat{n}\ dS \tag{2-3}$$

Blevins identifies the potential function for the flow over a sphere with radius of R as:

$$\phi(r,\theta) = U_0\left(r + \frac{R^3}{2r^3}\right)\cos\theta \tag{2-4}$$

With the potential function known for the flow surrounding a spherical mass, the Navier-Stokes equation can be used applying the potential equation's properties for the purpose of calculating the pressure along the spherical mass. Under the assumption of an inviscid fluid the Navier-Stokes equation can be re-written as:

$$\nabla\left(\frac{\partial\phi}{\partial t} + \frac{1}{2}V^2 + \frac{p}{\rho}\right) = 0 \tag{2-5}$$

This gradient's argument can be inferred to equal to a constant in space or a function of time $F(t)$. Thus Blevins states the pressure as,

$$p = \rho_f\left(F(t) - \frac{\partial\phi}{\partial t} - \frac{1}{2}V^2\right) \tag{2-6}$$

The inline force integral requires the normal vector and $d\boldsymbol{S}$ to be calculated. Because the principal mass affected is a sphere, Figure 1 geometrically projects the simpler evaluation via spherical coordinates.

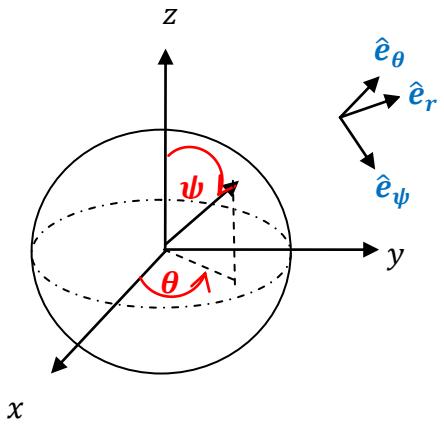

Fig. 1 Spherical coordinate system of sphere mass

With the normal vector to the surface of this sphere mass will be directed in the same manner as the $\hat{e}_r$ vector. The infinitely small surface can be defined as a cross sectional area for dS and completing the components necessary to evaluate F_x.

$$F_x|_{r=R} = \int_0^{2\pi}\int_0^{\pi}\left(\frac{3}{2}\dot{U}R\cos\theta + \frac{9}{8}U^2\sin^2\theta\right)\hat{e}_r\, R\sin\theta\, d\theta\, d\psi$$
$$= \underbrace{\frac{4}{3}\pi R^3\rho\dot{U}}_{Buoyancy\ Term} + \underbrace{\frac{2}{3}\pi R^3\rho\dot{U}}_{Added\ Mass\ term} \tag{2-7}$$

The buoyancy for a sphere is accurately represented through this derivation, revealing the force of the mass displaced by the volume of the fluid at the flow acceleration. The added mass phenomenon holds true to reveal Blevins added mass equation as a force per length [3]. However integrated over a length dimension would result in total linear force exerted at surface of the spherical mass. Thus Blevins equation can be re-written two different ways,

$$F_{A.M.per\ Length} = C_a \rho A \dot{U}$$
$$F_{A.M.} = C_a \rho V \dot{U} \tag{2-8}$$

By calculating and applying the previous equation it can be calculated to be composed of the accumulation of these forces result in the net fluid forces applied.

E. Hamilton's Principle via Lagrange's Method

Classical kinematics can come to a struggle to define this anemometer's motion along the beam length due to the continuous with several degrees of freedom. As another solution better suited to incorporate a continuous body, Hamilton's principle will derive a set of differential equations of motion of the given system using generalized coordinates. Hamilton's principle allows for the use of the Lagrangian, the basic building block for using Lagrange's Method.

Both theories along with the inline fluid forces present in the wind model will be applied to the Euler-Bernoulli beam theory in the following chapter.

CHAPTER III

DEVELOPING EQUATIONS OF MOTION FOR SPHERE ANEMOMETER

A. Spherical Anemometer Proposal

The wind forces previously summarized provided a better understanding of the influence a sphere anemometer is expected to undergo. The task of designing this anemometer is first diagrammed in Fig. 2, such that the body, motion, and forces of this hybrid system will need to be designed. The vertical shaft as in previous sphere anemometers is important in supporting and influencing the deflection of the sphere mass. A beam with stiff bending capability such as that of a Timoshenko beam would encompass the motion and stresses in various dimensions. However for the purpose of a simple wind model, with minimum turbulence and vorticity, a simplified Timoshenko beam, the Euler-Bernoulli beam, will neglect shear strains and torques. The Euler-Bernoulli beam as a result satisfies the criteria of the continuous body. A single dimension of deflection can now be the focus for the design of this anemometer. The proposal for the spherical anemometer is diagrammed below:

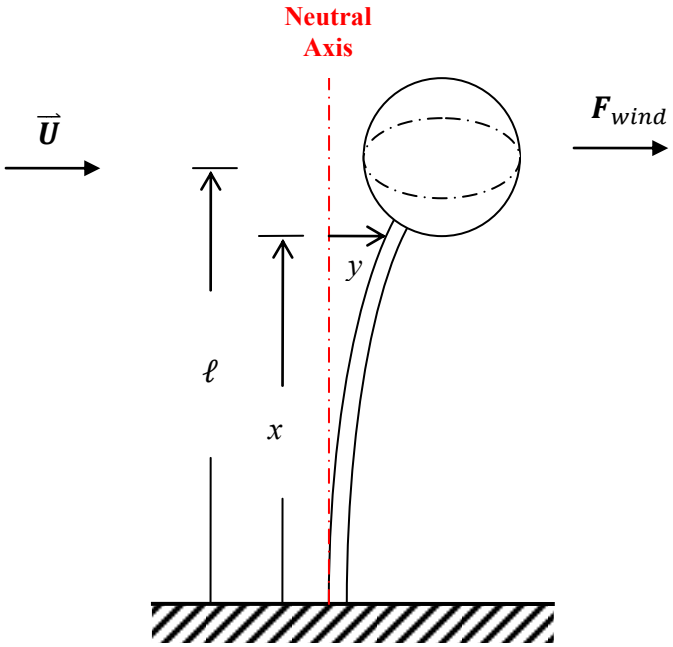

Fig. 2 Sphere anemometer diagram

The diagram depicts the motion of the spherical anemometer with a steady wind flow $\vec{U}$. The motion of the beam and spherical mass according to Euler-Bernoulli theory varies by two parameters: the position along the beam, x, and traditional time variable. This Euler-Bernoulli Beam has deflection y, total length ℓ, linear mass density ρ_b, Inertia *I*, and stiffness *E*.

B. Euler-Bernoulli Beam Derivation

1. Lagrange's Method

The Lagrange's Method identifies the contributing energies of the system to calculate the Lagrangian. The hybrid system's energy contributions come from both the

beam and sphere's kinetic and potential energies. Because of the assumption to use a cantilevered Euler-Bernoulli beam, torsion influences can be ignored and bending occurs in a single plane. Thus, deflection along the continuous rigid beam will be parallel to the wind direction. The motion of the sphere mass moves together with the beam's end and thus its speed is equivalent to the beam at the tip. Both the speed of the beam and the speed of the mass sphere can be identified as $\dot{y}(x,t)$ and $\dot{y}(\ell,t)$ respectively. Therefore the kinetic energies are:

$$T_{beam} = \frac{1}{2}\int_0^{\ell} \rho_b \dot{y}(x,t)^2\, dx$$

$$T_{sphere} = \frac{1}{2} m_{sphere} \dot{y}(\ell,t)^2 \tag{3-1}$$

Similarly, this beam's potential energy will be composed of the elasticity of material, second moment of inertia, and deflection along the entirety of the beam. The spherical mass is a rigid body with a constant potential energy in the deflection of the beam for small deflections thus only the beam contributes to the dynamic potential energy, **V**.

$$V_{beam} = \frac{1}{2}\int_0^{\ell} \mathrm{E}\mathrm{I} y''^2\, dx \tag{3-2}$$

2. Lagrangian for Hybrid Body

The Lagrangian is considered the difference in kinetic minus potential energy; however, a complete system can be composed of discrete, continuous, and boundary

parts. Thus we can develop Hamilton's Principle further with the full Lagrangian known as:

$$\mathcal{L} = \int_C L_C + L_B \tag{3-3}$$

In this beam's case, the complete Lagrangian only has continuous and boundary components due to the lack of a discrete component in the cantilevered beam system. The continuous part here corresponds to the kinetic and potential energy along the length of the beam. The boundary part corresponds with the mass tip's properties.

As described in the previous section the main wind force will be applied upon the spherical mass at the beam's end and thus produce work energy in the anemometer system. For the development of the following PDE equations, the non-potential work W_{np} will influence the energy contributions for the hybrid system and thus the Lagrangian. The non-potential forces in this system consist of the combination of inline wind forces. Therefore,

$$W_{np} = F_{wind} y(\ell, t) \tag{3-4}$$

W_{np} only represents the non-potential forces acting at the length of the beam, specifically the mass tip. The development of Euler Bernoulli Beams complies with the Lagrange-D'Alembert Principle, which states the following:

$$\delta L = \delta T - \delta V \tag{3-5}$$

The Lagrangian, L, is expressed in terms of a variation by the δ operator. This satisfies the equation made possible by Hamilton's Principle. Thus variation of the Lagrangian in conjunction with Hamilton's Principle states:

$$0 = \int_0^t \delta L - \delta W_{np}\, dt = \int_0^t \delta T - \delta V - \delta W_{np}\, dt \tag{3-6}$$

Because of the hybrid system, the satisfying equation will be applied to the corresponding parts of the system. A note should be made that there is a distinct difference in the time derivative used with the kinetic terms and the spatial derivatives appearance with the potential term.

$$\begin{aligned}\int_t \delta\,\mathcal{L} \;=\; & \int_t \delta\left\{\frac{1}{2}\int_0^\ell \rho_b \dot{y}(x,t)^2\, dx + \frac{1}{2} m_{sphere}\dot{y}(\ell,t)^2 - \frac{1}{2}\int_0^\ell \mathrm{EI}y''^2\, dx \right. \\ & \left. -\; F_{wind}y(\ell,t)\right\} dt \\ = & \int_t \int_0^\ell \rho_b\big(\dot{y}(x,t)\;\delta\dot{y}(x,t)\big)\, dx \;+\; m_{sphere}\dot{y}(\ell,t)\delta\dot{y}(\ell,t) \\ & -\int_0^\ell \mathrm{EI}y''\,\delta y'' dx - F_{wind}\delta y(\ell,t) dt\end{aligned} \tag{3-7}$$

In Equation 3-7, each kinetic and potential variation term prevent a traditional integration from being used; consequently, the integration by parts method will be used to progress the derivation process with either respect to time or length. Hurtado explains this process as one such that the boundary conditions specifically are produced per

implementation of integration by parts to the potential variation term [4]. The first boundary condition term, BC1, is produced from the first integration's boundary terms set to zero and the second boundary condition term, BC2, is a result of the second integration procedure. Next we show both BC1 and BC2 for further evaluation.

Boundary Conditions for Parameter $y(x,t)$:

BC1: $$-EIy''(\ell,t)\delta y'(\ell,t) + EIy''(0,t)\delta y'(0,t) = 0 \tag{3-8}$$

BC2: $$EIy'''(\ell,t)\delta y(\ell,t) - EIy'''(0,t)\delta y(0,t) - m_{sphere}\ddot{y}(\ell,t)\delta y(\ell,t) + F_{wind}\delta y(\ell,t) = 0 \tag{3-9}$$

By the definition of a variation such that $\delta y(x,0) = \delta y(x,t) = 0$. By following Figure 2, the first two boundary conditions are set for this cantilevered beam.

BC3 : $$y(0,t) = 0$$

BC4: $$y'(0,t) = 0 \tag{3-10}$$

BC3 and BC 4 infer the fixed end of the beam having zero deflections and zero slopes respectively at all times. Applying these conditions to the first two boundary conditions allows for the bending moment and shear moment to be identified as shown below:

BC1: $$EIy''(\ell,t) = 0 \tag{3-11}$$

BC2: $$EIy'''(\ell,t) = \ F_{wind} - \ m_{sphere}\ddot{y}(\ell,t)$$

As a result Equation 3-7's integral terms simplify to:

$$\int_t \delta\,\mathcal{L}\,dt = \int_0^t \int_0^\ell \rho_b \ddot{y}(x,t)\ \ \delta y(x,t) + \mathrm{EI}y''''\,\delta y(x,t)\,dx\ \ dt\ = 0 \qquad (3\text{-}12)$$

3. Non-Homogenous vs. Homogenous

The homogenous partial differential equations lie in the integral of Equation 3-12. Along with this PDE, the set of non-homogenous boundary conditions in Equations 3-10 and 3-11 accompany the equations. The shear boundary condition is mostly affected by the sphere mass at length ℓ of the beam and thus is not equal to zero. In order to apply modal analysis to the PDE's, the equations are rewritten by use of the Dirac delta function. The Dirac delta function allows for the third boundary condition to be re-written such that:

$$\rho_b \ddot{y} + \mathrm{EI}y'''' \ = \ F_y(x,t)\delta^D(x - \ \ell) \qquad (3\text{-}13)$$

With homogenous boundary conditions,

$$y(0,t) = 0\,; \quad y''(\ell,t) = 0\,; \quad y'(0,t) = 0\,; \quad y'''(\ell,t) = 0\,; \qquad (3\text{-}14)$$

C. Implementing Fluid Forces

1. Applying Buoyancy, Added Mass, and Drag

According to the buoyancy equation our buoyancy force will be,

$$F_B = \rho_f V \dot{U} \tag{3-15}$$

Considering the anemometer is exposed to wind resistance and air's fluid properties, Blevins Added Mass component applies to the deflected beam. The scenario best fits the added mass phenomenon in an accelerating fluid case. So the added mass force is,

$$F_{AM} = C_a \rho_f V (\dot{U} - \ddot{y}) \tag{3-16}$$

In both equations, ρ_f indicates the density of air, V is the volume of the mass tip sphere exposed to the wind environment, U is the wind speed, and $\ddot{y}$ is the mass acceleration. The third component, which this anemometer will be exposed to, is the drag force. The drag is calculated in a similar fashion to Blevins' Galloping and Fluttering cases for the point mass examples he studies. A relative form of the drag force is introduced by Blevins to factor large body accelerations,

$$F_D = \frac{1}{2} \rho_f |U - \dot{y}| (U - \dot{y}) A C_D \tag{3-17}$$

These three force components equate to a total wind force $F_{y\,wind}$ representative of the force affecting the anemometer's mass tip in the non-homogenous differential equations of motion derived beforehand.

$$F_{y\,wind} = F_B + F_{AM} + F_D$$
$$F_{y\,wind} = \rho_f V\dot{U} + C_a\rho_f V\left(\dot{U} - \ddot{y}\right) + \frac{1}{2}\rho_f|U - \dot{y}|(U - \dot{y})AC_D \tag{3-18}$$

2. Separation of Variables

The concept of separation of variables is considered for the case of the Euler-Bernoulli beam due to the partial differential equations subject to two parameters. The first assumption made is:

$$y = X(x)T(t) \tag{3-19}$$

Then the Euler Bernoulli equation $\rho_b\ddot{y} + \mathrm{EI}y'''' = 0$ where $\rho_b$and EI are constant beam property values. Substitution leads Equation 3-19 to:

$$\rho_b\ddot{T}X(x) + \mathrm{EI}\,T(t)X'''' = 0 \tag{3-20}$$

The first step for the separation process involves solving for the spatial component $X(x)$ by division of $\rho_b T(t)$:

$$\frac{\ddot{T}}{T} + \frac{\mathrm{EI}}{\rho_b}\frac{X''''}{X} = 0 \tag{3-21}$$

By introducing $\tilde{c}^2$ as a constant equal to $\frac{\mathrm{EI}}{\rho_b}$, then the variable β can be defined as the harmonic frequency to satisfy the orthogonal function $\mathrm{X}(x)$ in equation

$$\frac{\ddot{T}}{T} = -\tilde{c}^2 \frac{X''''}{X} = -\lambda^2$$

$$X'''' - \frac{\lambda^2}{\tilde{c}^2} X = 0 \;\&\; \frac{\lambda^2}{\tilde{c}^2} = \beta^4 \xrightarrow{yield} X'''' - \beta^4 X = 0 \tag{3-22}$$

This procedure yields a function with four orthogonal terms.

$$X(x) = c_1 \cosh(\beta x) + c_2 \sinh(\beta x) + c_3 \cos(\beta x) + c_4 \sin(\beta x) \tag{3-23}$$

If we recall the conditions of our non-homogenous partial differential equations with homogenous boundary conditions, then we can re-state the boundary conditions in Equation 3-14 with $X(x)$ definition in Equation 3-23.

$$y(0,t) = 0 = X(0)T(t) = c_1 + 0 + c_3 + 0$$

$$y'(0,t) = 0 = X'(0)T(t) = 0 + c_2 + 0 + c_4$$

$$y''(L,t) = 0 = X''(L)T(t)$$

$$= c_1 \cosh(\beta L) + c_2 \sinh(\beta L) - c_3 \cos(\beta L) - c_4 \sin(\beta L)$$

$$y'''(L,t) = 0 = X'''(L)T(t)$$

$$= c_1 \sinh(\beta L) + c_2 \cosh(\beta L) + c_3 \sin(\beta L) - c_4 \cos(\beta L) \tag{3-24}$$

Equations 3-24 entail not just $c_1, c_2, c_3,$ and c_4 as unknowns to solve but also the β variable. This β is representative of the resonance frequency for the hybrid system.

Thus, if $c_1, c_2, c_3,$ and c_4 can be calculated by a system equations that can be analyzed individually via the matrix representation of the system of equations [A][C] = [0], where [A] is a 4x4 coefficient representation of our four equation listed above, [C] = $[c_1, c_2, c_3, c_4]^T$, and [0] is a 4x1 matrix of zeros. Solving this problem requires using the properties of a determinant to set [A] to be a singular matrix (determinant equals zero) to satisfy the 4 applied boundary conditions of Equations 3-24. Because β is left as an unknown in the system the following infinite solutions can be produced from the resulting statement:

$$\cosh(\beta L)\cos(\beta L) + 1 = 0 \tag{3-25}$$

While Equation 3-25 reveals solutions for β, there are infinite frequencies to choose from. For the purpose of this work only the first three harmonics or available frequencies will be included. For future works additional frequencies could be used.

To solve for $T(t)$ we can re-write $X(x)$ as,

$$X(x) = \sum_i X_i(x) \;\; for\; i = 1,2 \ldots N \; where \; N = \#\; harmonics \tag{3-26}$$

Now we can define $y(x,t) = \sum_i X_i(x)T_i(t)$ or y = $X_i T_i$ via index notation. This method proves efficient in the uncoupling procedure for a *T(t)* solution, the expansion and the calculation of $X(x)$. As stated earlier, the beam's PDE and wind force are re-written when applied to Equation 3-13 with the new definition for the loading force:

$$F_y\,(x,t) = F_{y\,wind} - m_{sphere}\ddot{y} \tag{3-27}$$

$$\rho_b \ddot{T}_j X_j + EI\; T_j X_j'''' = \left\{F_{y\,wind} - m_{sphere}\ddot{T}_j X_j\right\}\delta(x-\ell) \tag{3-28}$$

In order to arrive at an ordinary differential equation for *T(t)* we follow the following: Multiply by X_i and integrate from $0 \rightarrow \ell$ for both sides,

$$\int_0^{\ell} X_i\{\rho_b \ddot{T}_j X_j(x) + EIT_j(t)X_j''''(x)\}\, dx = \int_0^{\ell} X_i\{F_{y\,wind} - m_{sphere}\ddot{T}_j X_j\}\, \delta(x-\ell)dx \tag{3-29}$$

In Equation 3-23 $X(x)$ was defined as an accumulation of orthogonal components or eigenfunction expansions in Sin, Cos, Sinh, and Cosh [5]. Thus according, to Byrne's definition of orthogonal functions via inner spaces the harmonics of X can be subject to the orthogonal condition [6]. Below we can apply the inner space product to the spatial function:

$$\int_0^{\ell} \hat{X}_i \hat{X}_j\, dx = \delta^K{}_{ij} \tag{3-30}$$

Here $\hat{X}$ represents a normalized $X(x)$. For normalization, each individual X harmonic will need to be normalized. For example using the variable D to normalize the first X as follows:

$$\int_0^{\ell} X_1 X_1\, dx = D\,; \quad \hat{X}_1 = \frac{1}{\sqrt{D}} X_1 \tag{3-31}$$

For simplicity of notation the normalized notation will be withheld from the following derivation but included in the simulation. Evaluating each term individually yields the following:

The LHS,

$$\int_0^{\ell} X_i \rho_b \ddot{T}_j X_j \, dx = \rho_b \ddot{T}_j \int_0^{\ell} X_i X_j \, dx = \rho_b \ddot{T}_j \, \delta_{ij} \tag{3-32}$$

$$\begin{aligned} \int_0^{\ell} X_i EI T_j X_j'''' \, dx &= EI \int_0^{\ell} T_j X_i X_j'''' \, dx \\ &= EI \, T_j \int_0^{\ell} X_i X_j'''' \, dx \overset{I.B.P.}{\Longrightarrow} EI \, T_j \int_0^{\ell} X_i'' X_j'' \, dx \\ &= \beta_j^4 EI \; T_j \delta^K{}_{ij} \end{aligned} \tag{3-33}$$

The RHS,

$$\begin{aligned} &\int_0^{\ell} X_i \{F_{y\,wind} - m_{sphere} \ddot{T}_j X_j\} \, \delta^D(x-\ell) \, dx \\ &= \int_0^{\ell} X_i F_{y\,wind} \delta^D(x-\ell) \, dx \\ &- \int_0^{\ell} \{X_i m_{sphere} \ddot{T}_j X_j\} \, \delta^D(x-\ell) \, dx \\ &= \int_0^{\ell} X_i F_{y\,wind} \, \delta^D(x-\ell) dx - m_{sphere} \ddot{T}_j X_i(\ell) X_j(\ell) \end{aligned} \tag{3-34}$$

The $F_{y\,wind}$ term can be recalled from Equation 3-18 to be a function of $U, \dot{U}, \ddot{y}, \text{and } \dot{y}$ terms, thus by substitution and application of definition of y from Equation 3-19 the terms become expandable.

Because of the drag force's use of a relative velocity, the absolute value presents further complexities towards the simplification of the theoretical derivation of these equations of motion. Experimentally and for simulation purposes an integrator will satisfy this condition without a problem. Eliminating the absolute value will be conditional by

For $U > \dot{y}$,

$$\int_0^{\ell} X_i \rho_f \left\{ V\dot{U} + C_a \rho_f V\left(\dot{U} - \ddot{T}_J X_j\right) + \frac{1}{2}\rho_f A C_D \left(U - \dot{T}_J X_j\right)^2 \right\} \delta^D(x - \ell) dx \tag{3-35}$$

First, $\dot{U}$ Term simplifies:

$$\rho_f V(1 + C_a)\dot{U} \int_0^{\ell} X_i\, \delta^D(x - \ell) dx = \rho_f V(1 + C_a)\dot{U} X_i(\ell) \tag{3-36}$$

Second, $\ddot{T}_J$ term:

$$\int_0^{\ell} X_i C_a \rho_f V\, \ddot{T}_J X_j\ \delta^D(x - \ell) dx\ = C_a \rho_f V \ddot{T}_J X_i(\ell) X_j(\ell) \tag{3-37}$$

Third, U^2 term:

$$\int_0^{\ell} X_i \frac{1}{2}\rho_f A C_D\, U^2 \delta^D(x-\ell)dx = \frac{1}{2}\rho_f A C_D\, U^2 X_i(\ell) \tag{3-38}$$

Fourth, $\dot{T}_J$ term:

$$\int_0^{\ell} \left\{ X_i \frac{1}{2}\rho_f A C_D\, 2\dot{T}_J X_j\, \delta^D(x-\ell) \right\} dx = \rho_f A C_D X_i(\ell) X_j(\ell) \dot{T}_J \tag{3-39}$$

Fifth, $\dot{T}_J \dot{T}_\iota$ term:

$$\int_0^{\ell} X_i \frac{1}{2}\rho_f A C_D\, \dot{T}_J X_j \dot{T}_k X_k \delta^D(x-\ell)dx$$

$$= \frac{1}{2}\rho_f A C_D \dot{T}_k \dot{T}_J \int_0^{\ell} X_i X_j\, X_k \delta^D(x-\ell)dx$$

$$= \frac{1}{2}\rho_f A C_D\, X_i(\ell) X_j(\ell) X_k(\ell) \dot{T}_k \dot{T}_J \tag{3-40}$$

Now our PDE equation becomes an ODE for T(t):

$$\left(\rho_b + m_{sphere} + C_a \rho V\right)\ddot{T}_j \delta_{ij} - \rho_f A C_D \dot{T}_j \delta_{ij} + \beta^2 E I T_j \delta_{ij}$$

$$= \rho_f V(1 + C_a)\dot{U} X_i(\ell) + \frac{1}{2}\rho_f A C_D\, U^2 X_i(\ell)$$

$$+ \frac{1}{2}\rho_f A C_D\, X_i(\ell) X_j(\ell) X_k(\ell) \dot{T}_j \dot{T}_k \tag{3-41}$$

3. Equations of Motion for Anemometer

The non-linear ODE that results from the equation above occurs when j =i = k,

$$\left(\rho_b + m_{sphere} + C_a\rho_f A\right)\ddot{T}_i - \rho_f AC_D\dot{T}_i + \beta^2 EIT_i$$

$$= G_1\left(U(t)\right) + G_2\left(\dot{U}(t)\right) + \frac{1}{2}\rho_f AC_D X_i(\ell)^3\dot{T}_i^2 \qquad (3\text{-}42)$$

Such that,

$$G_1\left(U(t)\right) = \frac{1}{2}\rho_f AC_D U^2 X_i(\ell)\,; \quad G_2\left(\dot{U}(t)\right) = \rho_f V(1 + C_a)\dot{U}X_i(\ell)\,; \qquad (3\text{-}43)$$

This non-linear differential equation now can be computationally solved or used for any other functions dependent upon the function of *T(t)* such as the strain function, $\varepsilon(x,t)$. The following section will develop the relationship between strain and the time-dependent function of the beam to give us a second order differential for strain.

4. From EOM PDE to Strain ODE

Measuring strain for the beam deflection will use a set of strain gauges to be placed strategically to give the best measurement of total bending moment and indicate direction. Through implementation of a Wheatstone bridge, a stress placed on the strain gauge will cause a change in length of resistors. Thereby a change in resistance is given by the equation,

$$G.F. = \frac{1}{\varepsilon}\frac{\Delta R}{R}\,; \qquad \varepsilon = \frac{\Delta L}{L}\,; \qquad (3\text{-}44)$$

The gauge factor, G.F., is an abbreviation for a constant value of a strain gauge expressing a relation in resistance and length.

According to Young's Modulus strain is related to stress by,

$$\sigma = E\varepsilon \quad \varepsilon = \frac{\sigma}{E} = \pm c\frac{\partial^2 u}{\partial x^2} \tag{3-45}$$

The function u is the deflection equation for the beam in Equation 3-18 and c is the displacement of the strain gauge from the central axis of the beam's center, in this particular research it will placed on the outside of the beam thus, c will reflect the magnitude of the beam's radius.

Thus,

$$\varepsilon_y = \pm c\frac{\partial^2 y}{\partial x^2} \tag{3-46}$$

By applying the separation of variable Equation 3-19 to relate between strain and the equations of motion for anemometer's beam,

Accordingly we can find ε_y, $\dot{\varepsilon}_y$, and $\ddot{\varepsilon}_y$

$$\varepsilon_y(x,t) = c\,X''(x)T(t)\,; \quad \dot{\varepsilon}_y(x,t) = c\,X''(x)\dot{T}(t)\,;$$

$$\ddot{\varepsilon}_y(x,t) = c\,X''(x)\ddot{T}(t)\,; \tag{3-47}$$

We will define

$$X_* \stackrel{\text{def}}{=} X|_{x=x_*}\ ;\ \varepsilon_{y_*} \stackrel{\text{def}}{=} \varepsilon_y\big|_{x=x_*} \tag{3-48}$$

By some algebraic coefficient multiplication we can use ε_{y_*} to create a second order differential:

$$\frac{\left(\rho_b + m_{sphere} + C_a \rho_f A\right)}{c\, X_*''} \ddot{\varepsilon}_{y_*} - \left(\frac{\rho_f D C_D}{c\, X_*''}\right) \dot{\varepsilon}_{y_*} + \left(\frac{\beta^2 EI}{c\, X_*''}\right) \varepsilon_{y_*}$$

$$= G_1\big(U(t)\big) + G_2\left(\dot{U}(t)\right)$$

$$+ \frac{1}{2} \rho_f D C_D\, X_i(\ell) \left(\frac{\dot{\varepsilon}_{y_*}}{c X_*''}\right)^2$$

(3-49)

This differential equation for the beam's strain is now a second order non-linear ODE dependent upon wind speed and acceleration. A computational solution of this differential can be integrated using MATLAB's ordinary differential equation solver. The preceding strain model however contains several parameters that have been briefly discussed but for the purpose of a future experiment a design method for several parameters will be detailed in the following chapter. This strain model thus will serve as the true model for the strain the sphere anemometer will undergo at X_*, the placement of a test strain gauge. For approximation of wind speed not all the parameters of Equation 3-48 will be available and thus another approximation will be discussed.

CHAPTER IV

CALCULATING WIND SPEED

The wind force loads and the derivations of the motion of the sphere anemometer have led to a strain model that can be used for simulation of the true strain per the theory implementations. The next phase for the wind speed approximation lays in the design of both the wind model and the physical anemometer parameter dimensions. As some theories have been applied earlier the same must be applied in the design of both environment and system to prepare the simulation.

A. Simulation Preparation

The anemometer simulation will be represented by using the strain model presented earlier, along with a theoretical strain gauge influenced by white noise to project realistic measurement errors with accuracy as Omega's SG-Series strain gauges. The wind model consists of a ramp function followed by a semi-steady state phase containing relatively small amplitudes of oscillation. This simulation will undergo a sixty second run time for the purposes of the following examples. Using the measurements from the theoretical strain gauge, the steady state equation will approximate the wind model $\widehat{U}$.

B. Wind Environment Model

For the given wind model there will two be two important phases for which the wind model will pertain to during simulation. These sections can be classified as a transient or a steady state. The transient state behaves as its name suggests for the initial ten seconds of the time window. This portion, unlike a steady state, has a fluctuation in wind speed and acceleration. During the transient phase, the anemometer is subject to all of the fluid forces previously derived and as a result maintains the complexity of the complete strain ODE. Although using the complete strain ODE would provide the best accuracy, an experimental setting would not be able to provide strain rates necessary for the higher order terms of the model. Because the strain gauge measurement involves white noise for this simulation, the strain rate cannot be approximated using the rates of the measurements. Consequently analyzing the steady state approach is the best fitting for wind approximations.

Thus the following simulations will be analyzed by an environment experiencing that a ten second wind transient state followed by an semi-ideal steady state experience with minor oscillations. To assume a steady state we will incorporate the $U(t)$ model as follows:

$$U(t) = \begin{cases} -1.5 * (t-10)^2 + 150, & t < 10 \\ 150 + g(t) \quad , & t \geq 10 \end{cases} \tag{4-1}$$

Where,

$$g(t) \sim A_{SS} * \sin(t) \tag{4-2}$$

The purpose of $g(t)$ is to simulate the slight oscillations, amplitude A_{SS}, that can occur during the steadiest phases of a wind environment.

During steady state conditions however the components necessary to approximate $\widehat{U}$ are simply compiled from the measured strain, $\hat{\varepsilon}$, without a need for the measured strain's rates since constant wind conditions will render $\dot{\hat{\varepsilon}}$, and $\ddot{\hat{\varepsilon}}$, negligible to zero in a perfect constant wind or an ideal steady state.

C. Euler-Bernoulli Beam Model

Several theories and approximations have already been assumed and made for simplicity purposes in modeling the vertical shaft for the spherical anemometer. The Euler-Bernoulli beam theory was adopted for this model; as a result, the physical parameters influenced will be constrained to a degree for the simulations to follow.

In chapter 2, the concept of an Euler-Bernoulli beam was introduced due to the favorable properties that prevent shear and other trans-axial strains from influencing the primary deflection of beam from neutral axis. The first constraint distinguishes the material composition of this beam. The theoretical beam (the experimental anemometer's shaft) is restricted to a small deflection to length ratio. A material with a high enough stiffness and density to prevent large deflections is required. This restriction is defined by Euler-Bernoulli's theory which cannot approximate accurately at large deflection ratios due to the associated non-linear motion. With AL6061's high density of 2700 kg/m^3 and Elastic

modulus upwards of 7 Giga-Pascal, the beam should maintain relative small deflections despite high wind speeds; consequently this aluminum alloy is proposed for testing.

However another essential parameter in an accurate model of an E.B's beam deflection pertains to maintaining a 10:1 length to width ratio. As a result, this assumption for length can be considered for the simulations.

$$L_{beam} \geq 20 * R_{beam} \tag{4-3}$$

The second approximation to be considered is the negligible drag force of the beam's normal surface area to the wind. The general thought is to make sure that the ratio of drag force upon the spherical mass to the drag force along the beam's length is large enough to deem the beam's length drag force negligible. Thus minimizing the continuous parameters of the beam's drag will leave a relatively small load across the length of the beam. For this reason only a drag force is loaded at the beam's end. The parameters to take into account are R_{beam}, L_{beam}, and R_{Sphere} as the most critical to affecting the surface area subject to the drag force. Using approximation for the negligible drag force of

$$F_{D_{beam}} = \frac{1}{2}\rho_f D_{beam} * C_{D_{cylinder}} * L_{beam} * U^2 \tag{4-4}$$

In contrast to the drag force applied at the beam's end, $F_{D_{beam}} \ll F_{y\,wind}$ will introduce another constraint to consider with design parameters. Ideally a decent approximation for this condition would suggest

$$F_{D_{beam}} = 10 * F_D \tag{4-5}$$

Applying Equations 4-3, 4-4, and 4-5 to F_D yields a direct relationship between the sphere's radius R_S and the beam's radius R_b. Equation 4-6 below shows this.

$$R_S{}^2 \geq \frac{80}{\pi} R_b{}^2 \tag{4-6}$$

Thus, this leaves the radii of beam and sphere mass variable to a degree of convenience and practicality. The beam's width however does need to be large enough to hold a basic strain gauge such as the SG-Series strain gauges by Omega, featuring a width ranging from 0.1 - 0.2 inches, depending upon the specific model [6,7].

Incorporating the previous consideration in conjunction with the drag force condition will allow for the following parameters to be set:

$$R_{beam} = 0.4", L_{beam} = 8", \text{ and } R_{Sphere} = 5.2"$$

Although, these parameters are higher larger in magnitude than other previous experiments, the strain gauge will be physically accommodated under these parameters.

D. Simulations

The simulation of the spherical anemometer is next tested with steady state wind conditions, variations in beam parameters, error magnitude per strain gauge, parameter uncertainty, and sampling frequency to accurately compare steady state responses and the respective wind approximations.

1. Introducing Strain Gauge Noise Parameters

The linear relationship between the motion, deflection of the beam, and the strain active along the beam is directly related by the scaled factor shown previously, thus the true strain can directly the strain model in Equation 3-49 by ode45's Rung-Kutta's method. In order to understand the effect and magnitude of strain to expect with the giving considerations our first simulation is the baseline model approximation as shown below:

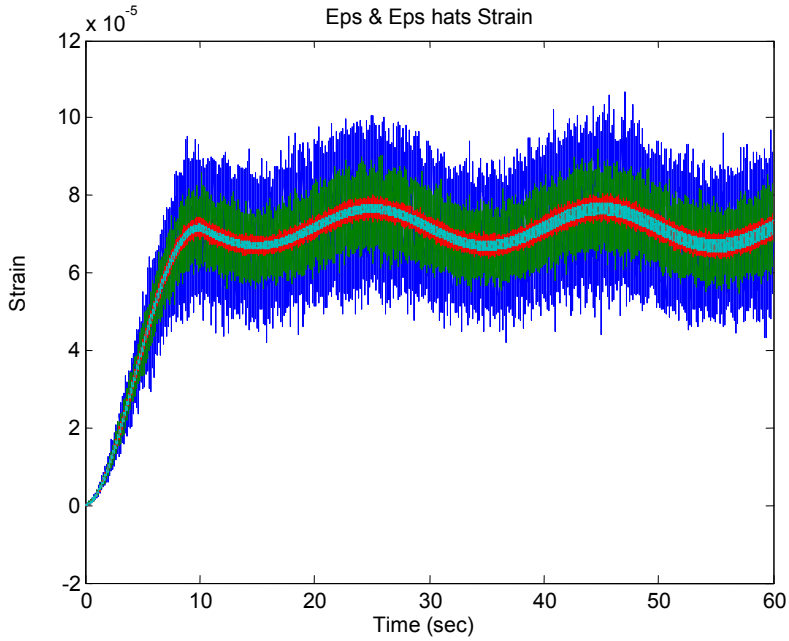

Fig. 3 Strain model according to steady wind oscillation

Figure 3 shows the complete collection of measured strains varied in error magnitude by a white noise application to the true strain model integrated by ODE45. Above the true strain model and the measured strains, following the standard deviation

of white noise by 1%, 5%, 10%. True strain, 1% error, 5% error, and 10% error and shown from thinnest to widest plots respectively.

Implementation of the Steady State equation for the approximation of $U, \widehat{U}$ specifically, is indicated below:

$$\widehat{U} = \mp \sqrt{\frac{2\left(\frac{\beta^2 EI}{c\, X_*''}\right)\hat{\varepsilon}_{y_*}}{\rho_f D C_D X_i(\ell)}} \tag{4-7}$$

This steady state approximation will allow for wind analysis with varying strain gauge noise.

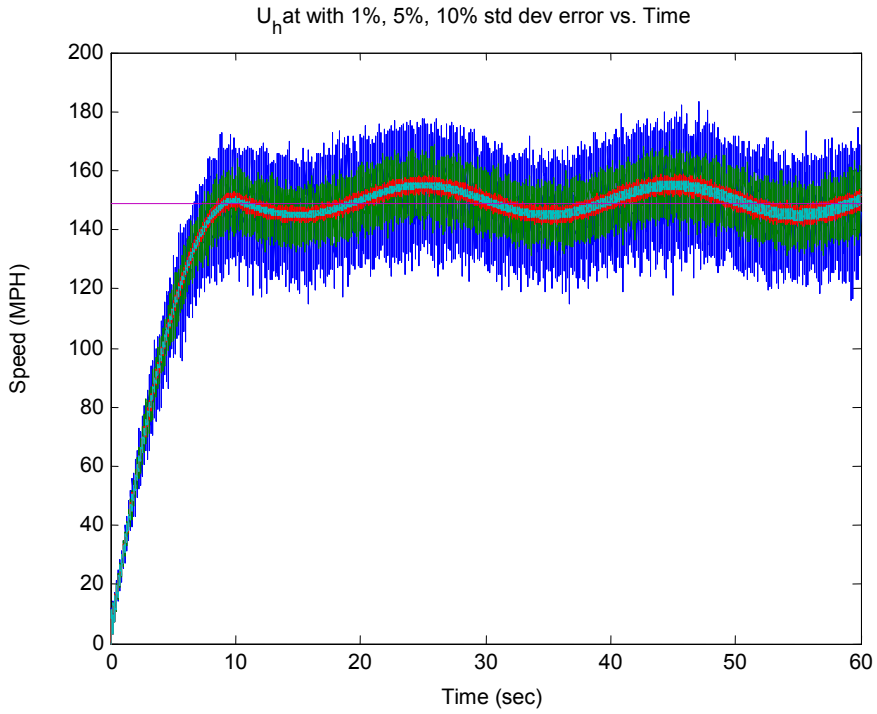

Fig. 4 Wind model approximations according to steady state

The wind approximations shown in Figure 4 reveal the effects of the strain gauge's accuracy. The additional straight line approximately shown at 150 mph is the U_{SS} calculated by means of an averaged window from t= 30 to 60 seconds. U_{SS} averages the measured strain during the steady state and thus can calculate a steady state approximation for the 30 second window span.

These calculations show the constant variance due to the high frequency in the strain measurements per point due to the non-fixed time steps of the Runge-Kutta method used. The large number of measurements leaves open the possibility to attempt averaging a set number of strain measurements and using the corresponding strain average to continuously update a wind approximation. Using this running average should help offset the white noise at the expense of a delay depending on the time window used.

2. Introducing Parameter Perturbation

Known parameters for experimental test can often be inaccurate to a degree due to numerous reasons such as calibration issues, physical dimension errors, equipment inaccuracies, etc. Parameter perturbation can be concerning in these simulations as well if the true strain for the anemometer is not exact due to a slightly longer beam, heavier density material, or even inaccurate coefficient for drag.

The purpose of the following simulations involves modifying the individual parameters of the strain steady state equation and observe significant changes if any.

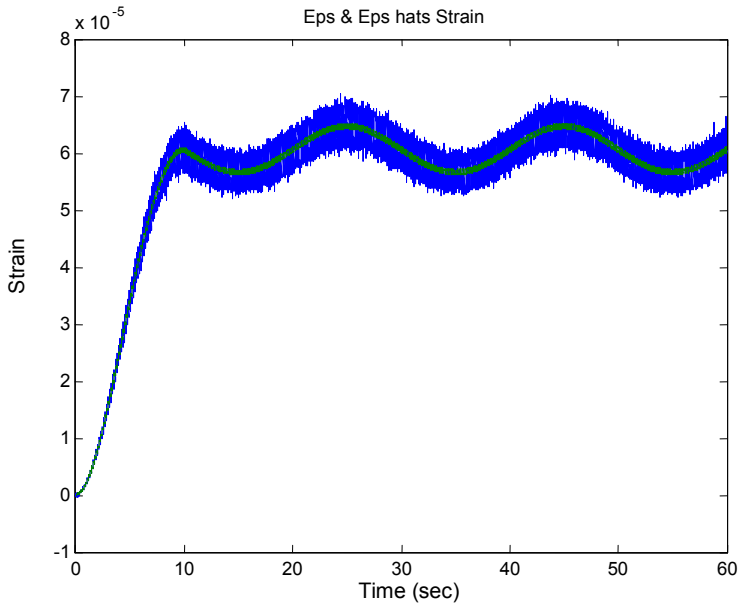

Fig. 5 Strain model magnitude

The original method is displayed in Figure 5, without parameter perturbation and $\widehat{U}$ following the similar oscillation of the true wind model and averaging nearly 150 mph.

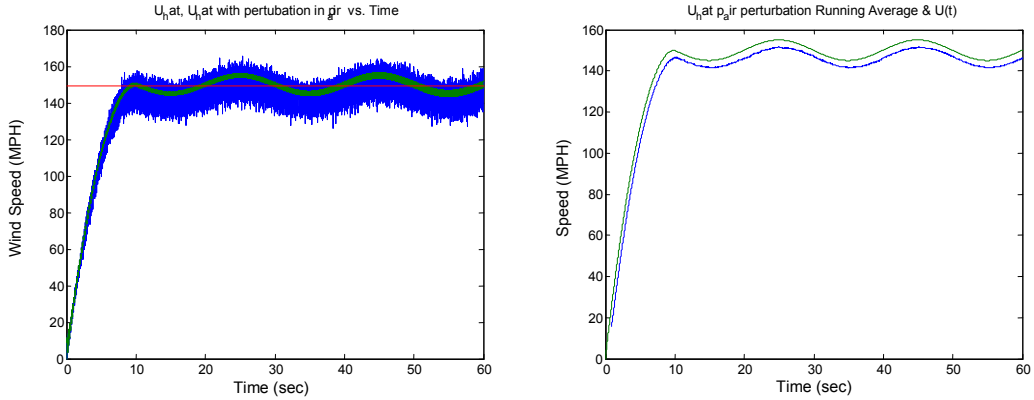

Fig. 6 Perturbation of $\boldsymbol{\rho_{air}}$

Figure 6 shows the effects of modifying the density of air, C_D, or distance to strain from center of beam, having an error of up to 5%, gives a result very similar in characteristic to the original calculation for $\widehat{U}$. However, the exception in results is a constant under approximation by 4 mph.

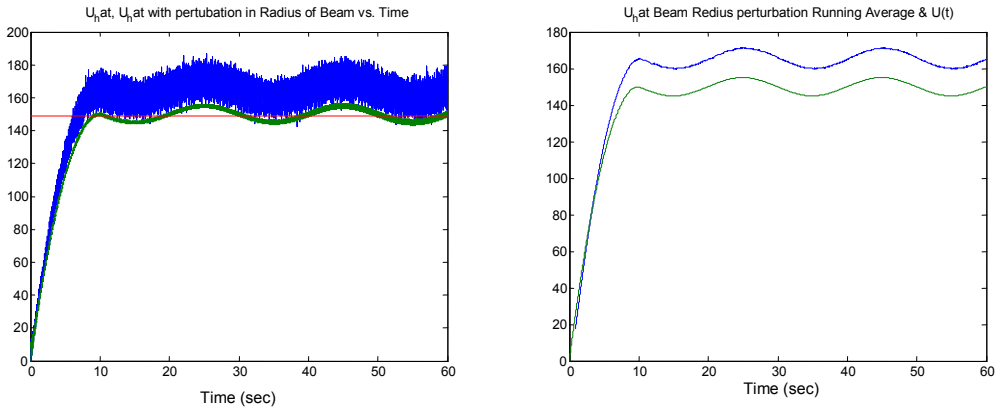

Fig. 7 Perturbation of beam radius

Radius of the beam proves to be one of the most significant and dramatic changes in wind approximation results. Figure 7 shows how a 5 % error in the beam's radius is capable of a -15 mph or -10% errors in wind approximation. Through perturbation of the beam's radius it can be inferred that radius length does have at least a fourth order exponential influence upon the steady state equations.

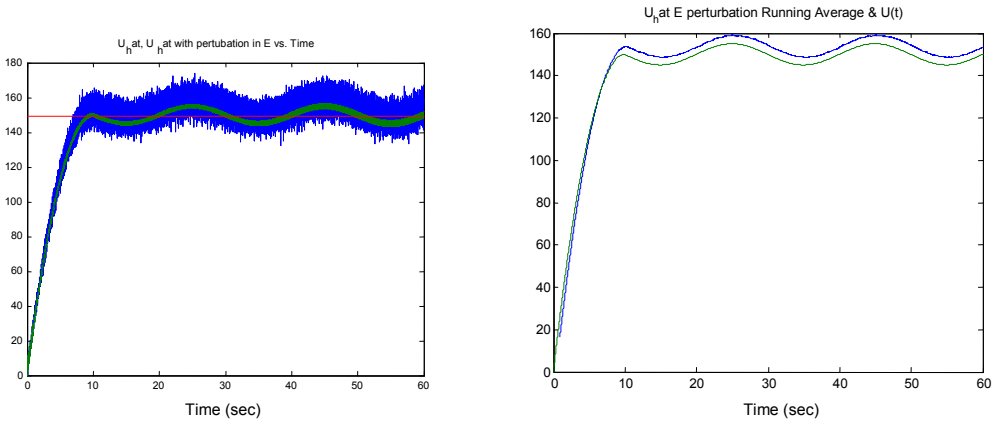

Fig. 8 Perturbation of elasticity

The Elastic modulus parameter for the beam as a result has an approximate 4 mph deviation from the true model due to the single linear contribution to the steady equation. Thus, Figure 8 shows that a 5% perturbation only causes a 2.7% alteration to $\widehat{U}$.

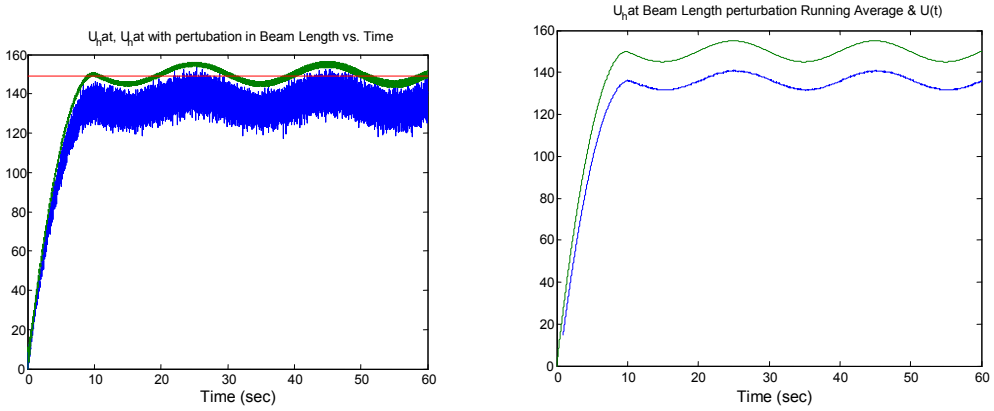

Fig. 9 Perturbation of beam length

Figure 9 specifically focuses upon the effect a 5% overestimation of the Beam's length can have a -8% influence of $\widehat{U}$.

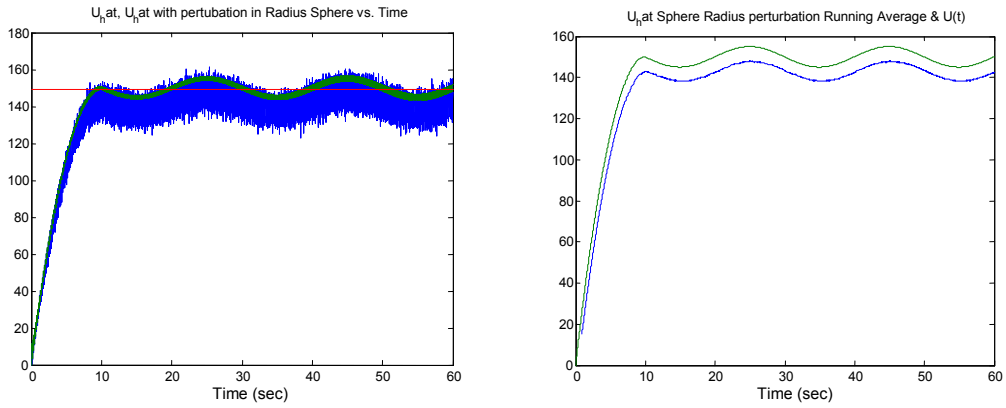

Fig. 10 Perturbation of sphere radius

Figure 10's slight estimation errors are shown above due to perturbations of sphere radius.

3. Introducing Average Window Method

Because of the high frequency in MATLAB's ODEs having a running average window can take a width of readings and average $\widehat{U}$ for a rolling time span which in effect will average the strain gauges white noise that can interfere with estimating accuracy of $\widehat{U}$. Shown below in Figure 11 the imminent difference is shown:

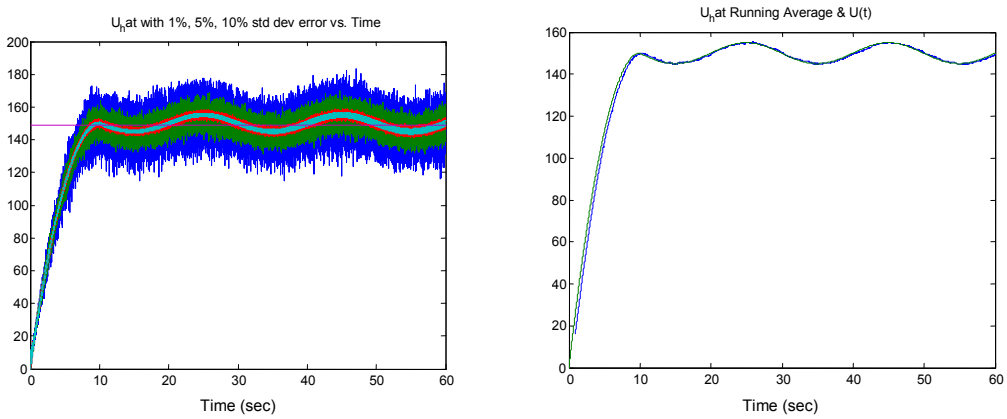

Fig. 11 Wind estimate with strain gauge noise 1%, 5%, 10%

Figure 12 provides an updated plot of the new comparison in the approximation U_{avg} to the true wind model. The first observation is clearly the reduction in noise. The slight delay is evident however for these purposes the delayed model betters the previous U approximation model.

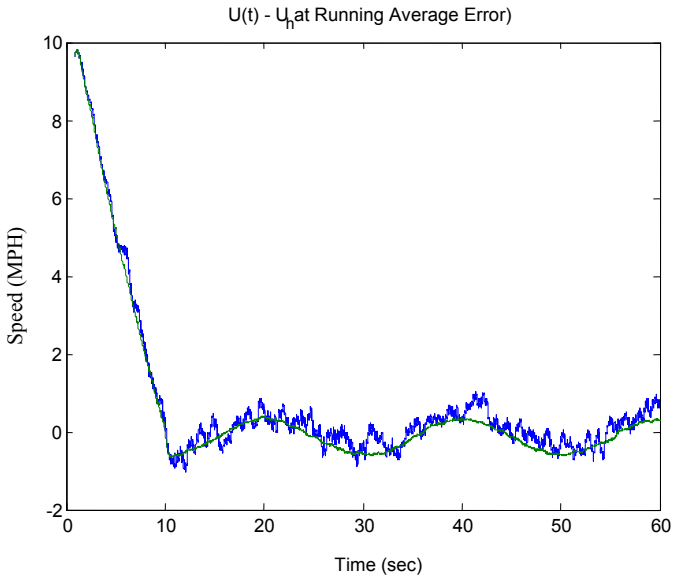

Fig. 12 Wind estimate average method error

Comparing the difference in the high error and low error difference with respect to the true wind model shows the higher and distinct error noise involved with the 10% error plot. Another observation to be noted involved the low magnitude in error along steady state and the lack to capture the complete transient state. The absence of the strain rates and wind rates are unknown during the transient phase and thus our steady state model fails to adequately capture a complete wind approximation.

4. Introducing Frequency Sampling

The simulations so far have been performed under the specification of a running average with a set time window which allows for better results in exchange for a time delay or lag in simulations. For the purpose of our work the lag is not a concern since specific time of occurrence is negligible compared to accuracy of actual wind speeds achieved. For a brief a analysis of the simulations high sampling frequency, required by Runge-Kutta4 for integration purposes at equal time intervals, the simulation is set to be sampled at the original 1600 Hz by the integrator down to 25 Hz. Later the implementation of a strain gauge implementation will use an even lower frequency but for the purposes of this analysis the wide range shows the significance of sampling. This allows us to explore the sampling frequencies of 1600 Hz, 800 Hz, 100 Hz, and 25 Hz for analysis.

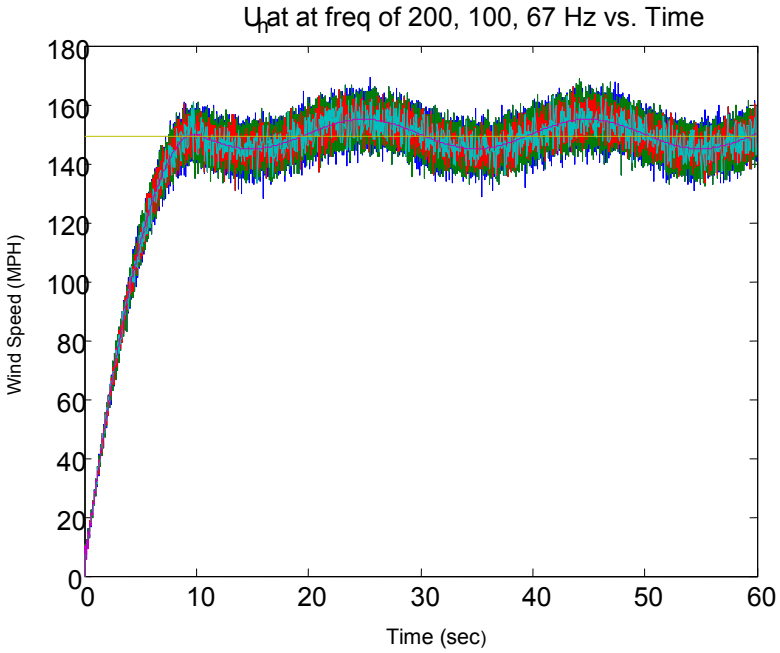

Fig. 13 Wind estimate via frequency sampling

The U approximations in Figure 13 tend to indicate the lower frequencies to be closer to the U(t) model; however, the high fluctuation in all of the sampled approximation models impedes an accurate conclusion. The wide range of +/- 10 mph does not provide with a reliable result to infer from. For this reason the running average is performed upon each sampled model:

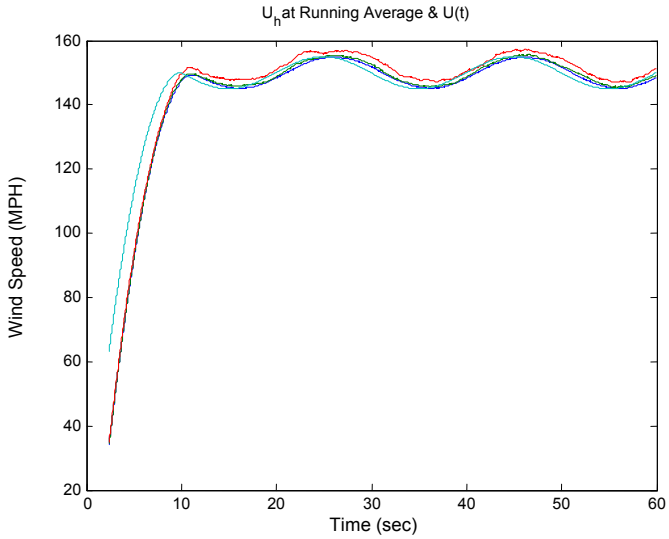

Fig. 14 Wind estimate of running average with sampled frequencies

The lag is clearer and visible from the original U(t) in Figure 14. We begin to see a difference now between the highly sampled and the least sampled models. For a better analysis, an error measurement will indicate the discrepancy.

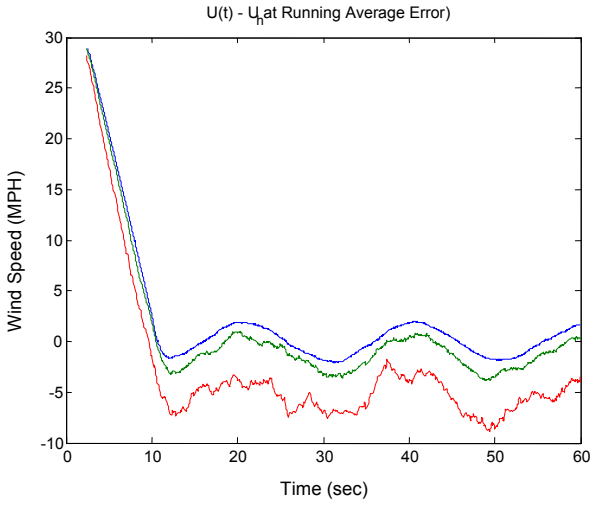

Fig. 15 Wind estimate with running average method error per frequency

Figure 15 is an error plot revealing the difference in our sampled approximations. Both of our sampled approximations were done a running average window of 2.4 seconds but the green data is lowered in frequency from 100 Hz to 50 Hz and the red model is lowered from 25 Hz to 12.5 Hz. The clear observation reveals an under sampled error deficiency where we can achieve numbers about 5 mph lower in a steady state due to a change in the sampling frequency.

5. Recording Data Methods: Real-time vs. Data Logger

Using a simulator such as MATLAB with an integrator such as ODE45 the number of points per second or sampling frequency can be very high in magnitudes particularly with the transient phase of the wind model reaching sampling frequencies up to 10 KHz. As a result using a fourth-order Runge-Kutta method can integrate with an evenly time-spaced frequency.

For an experimental setting the sampling frequency will be influenced by memory available for data storage and processing speeds of equipment. Unless working with real-time equipment or experimental equipment nearby, data loggers provide the best solution to have data stored to be retrieved at a later time. Utilizing equipment such as data loggers will require a sampling frequency no higher than 1 Hz. For this reason, the effect of frequency sampling will be examined for the wind approximation of the given wind models.

For the following cases a comparison between a 1000 Hz sampled approximation to a sampled approximation of the theoretical data logger under varying amplitudes in the steady state oscillations. Under steady state oscillations without amplitude, the wind approximation stays within +/- 2 mph or (1.4 % of U)

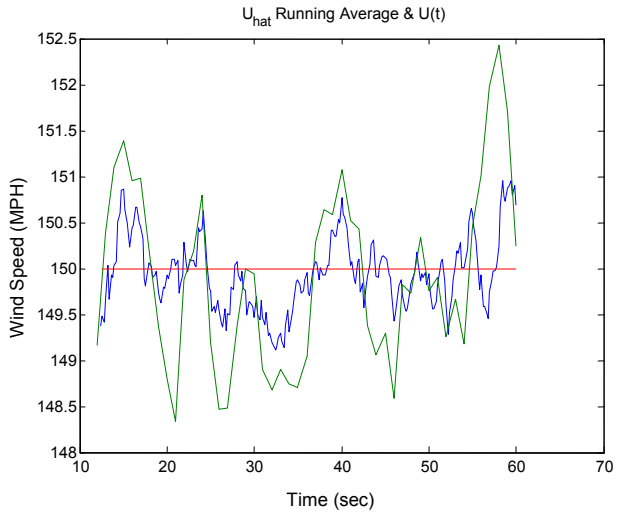

Fig. 16 Wind estimate running average method with data logger

The green data plot of Figure 16 shows the data logger sampling compared to the wind model. Under oscillations with amplitude set to 5:

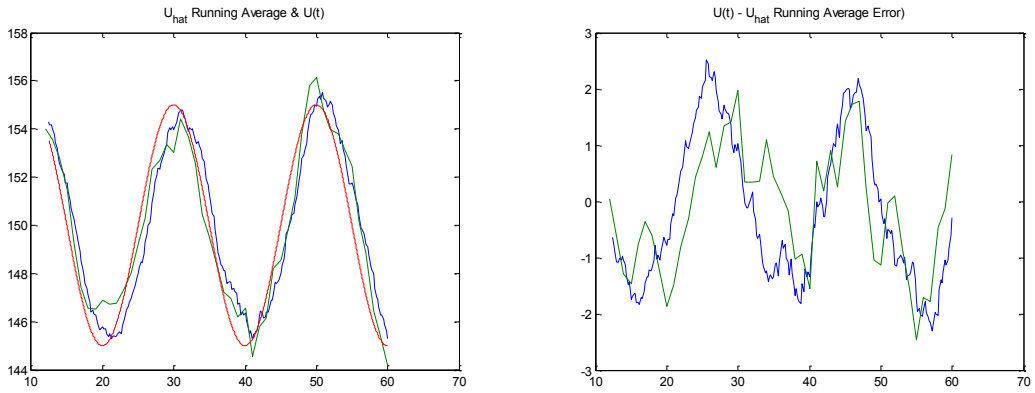

Fig. 17 Wind estimate with data logger and amplitude of 5 mph

The sampled data logger of Figure 17 approximates wind speeds within a +/- 2.3 mph (about 1.5% U error) Under oscillation with amplitude of 15:

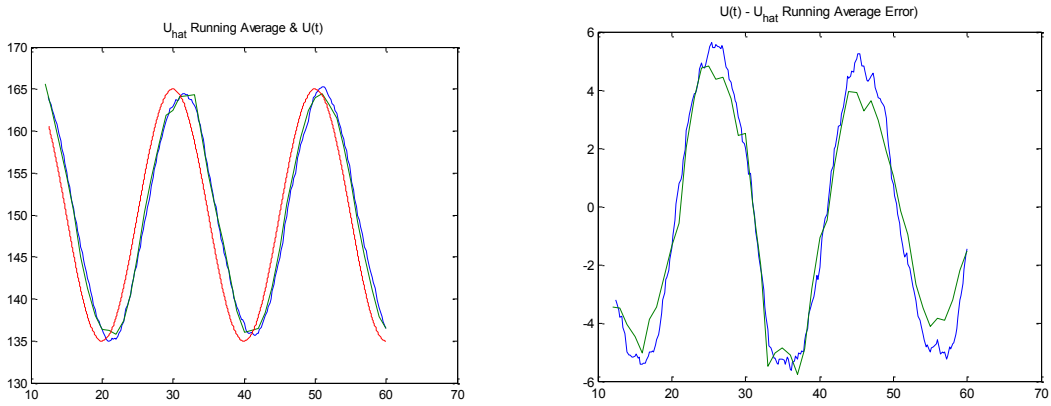

Fig. 18 Wind estimate with data logger and amplitude of 15 mph

With a 15 mph amplitude (10% wind oscillation), the data logger in Figure 18 is accurate to approximately +/- 5 mph (3.3% of U value).

CHAPTER V

DISCUSSION

Simulation performances by the steady state strain model for high speed wind were approximately analyzed for accuracy. Sampling frequency, steady state wind model, averaging window method and parameter perturbation was tested in Chapter 4. Strain measurements are designed by following the characteristics of a white noise subject to a standard derivation of a magnitude high enough to ensure satisfying the standard tolerances of Omega's strain gauge specifications [7].

A. Full-Bridge Strain Gauge Implementation

Chapter 4 showed how measurement error was applied due to strain error which was estimated by a white noise with a tolerance between 1-5%.

National Instruments details the important resistance change and thereby strain by the schematic implementation of a Wheatstone bridge with simply one main resistor representing a strain gauge up to all four active resistors representing four strain gauges. This difference represents a quarter-bridge strain gauge model and the full-bridge strain gauge respectively.

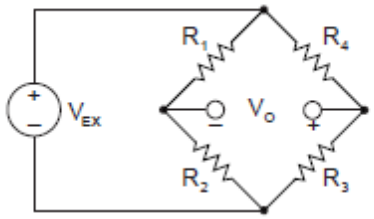

Fig. 19 Simple wheatstone bridge [6]

In Figure 19, the external voltage V_{EX} yields no output voltage V_O if $R_1 = R_2 = R_3 = R_4$.

$$V_O = \left[\frac{R_3}{R_3 + R_4} - \frac{R_2}{R_2 + R_1}\right] \cdot V_{EX} \tag{5-1}$$

However with stain gauge application in conjunction with Equation 3-43 will yield variable resistance for R_i. According to a National Instruments' tutorial,

$$\Delta R_i = R_{G_i} \cdot GF \cdot \varepsilon \tag{5-2}$$

Here R_{G_i} will refer to the nominal resistance per strain gauge, GF is the constant Gauge Factor, and ε the compressed or tensed strain [7].

To have a better understanding of exactly how the strain may be calculated in an experimental setting, we carry out the following example for a full-bridge strain gauge realization.

For an experimental hardware setup the four strain gauges must be arranged for compression and tension purposes along the same position of the beam. Each strain gauge will have a nominal resistance and be accurate within +/- 0.5% according to

Agilent [8]. From an experimental setting the R_{G_i} of each strain gauge are assumed equal and thus,

$$\frac{V_O}{V_{EX}} = GF \cdot \varepsilon \tag{5-3}$$

The V_O is the only measurable variable thus,

$$\hat{\varepsilon} = \frac{\widetilde{V_O}}{V_{EX} \cdot GF} \tag{5-4}$$

This is the ideal case though where nominal resistance does not influence the strain reading. However the tolerance in nominal resistance can influence the actual strain of the Wheatstone bridge. Thus a statistical analysis could be implemented to simulated true strains and voltages to establish nominal resistance values not exactly equal and see how accurately the strain can still be represented by the output voltage function. Because the full strain gauge contains noise in the resistance but are combined in the voltage calculations, the noise should reduce with the higher number of combinations of strains in a compression/tension pair. This simulation would lead the ground work for typical voltages to look for and anticipate if tested in a wind tunnel with real time data analysis.

B. Water Energy Harvesting

Another growing purpose for investigation involves the use of waves and natural currents to create and store a clean and renewable energy source. Keeping track and optimizing the use of the water's natural to store energy would require a method of keeping track of the current's speed. A type of fluid anemometer is necessary in this case to keep track of the fluids changing speed.

To implement this idea several factors could play into effect such as the performance needs of such a fluid measuring device. Assuming the purpose is to provide a simple reading of water speed in a fairly steady environment; the spherical anemometer is submerged in water but could be designed in a similar fashion to the anemometer for wind. The fluid density is the top change in this environment from relatively small 1.8 kg/m^3 to magnitude of approximately 990 kg/m^3. One of the things to consider is how dynamic the water currents will be in terms of sudden currents changing from steady state. With the application of the running average method, the way the readings are recorded and the time lag will change to better fit the needs. Analyzing typical wave speeds will reveal a higher undergoing strain per fluid speed but overall lower fluid speeds in this scenario.

C. Modification of Frequency

Different weather services describe gusts of wind to be a distinctly higher wind speed held over a short time span of a few seconds. Thus the approximation model could

be expanded to accept steady wind models with oscillations spanning different lengths of time. An alteration in the frequency of gusts in an otherwise steady wind model could be analyzed for accuracy by data logger, as done in chapter 4, to see if the calculations are delayed. The calculations would still involve some approximations as with earlier examples. Because the recording frequency is approximately 1 Hz and gusts of wind are at least strong for a couple of seconds, oversampling is not a concern.

One other concern that may need to addressed when the environment model begins to diverge from the steady state model with not only higher oscillations but varying frequencies. For example a wind gust will not likely oscillate with the same period and strength in a normal environment. Thus wind gust could vary from very low frequencies to gusts of up to 3 seconds and maybe shorter. This could propose a need to make the model of the anemometer's resonance frequency is set to be much higher than that of the wind. Thus changing the physical properties would need to be optimized to increase frequency. One frequency factor is dependent upon the mass of the mass tip. However making the mass smaller would also reduce drag and other fluid forces. For this reason simulations with a hollow sphere could expand the opportunity to introduce wind gusts and continue broadening the capabilities of this anemometer.

D. Additional Dimension Analysis

Ideal flow was treated to a one dimensional constraint for simplicity but when experiencing realistic unknown wind direction and conditions, the sphere anemometer is subject to bending in a combination of directions.

A proposed solution would involve expanding the idea of half-bridge Wheatstone strain gauges. By placing at least two sets of Wheatstone Half-Bridges at the four quadrants of the sphere anemometer's beam at least two strain gauges will always be subject to tension and two to compression. The only exceptions would occur if the wind direction of $U(t)$ is directly perpendicular to a quadrant of the beam. For this case, an overall strain would have to be calculated by a vector-like combination of both strain gauge magnitudes.

CHAPTER VI

CONCLUSION

The approximation model of this research has provided a viable solution to implement a sphere anemometer under steady high wind speeds with modest accuracy. Although many linearized forces and assumptions were made for the purpose of an attainable ODE to integrate and test different setups; the accuracy of the strain model proved to be accurate with the filtering effect of an average time window for the wind speed approximation $\widehat{U}$.

The continued accuracy of the steady strain model proves to be better than expected despite large amplitude oscillation in wind environment. Parameter perturbation proved to be critical for the three physical parameter fit to satisfy the considerations of the anemometer design. The thickness of the beam of this Euler-Bernoulli revealed the strongest influence for the wind approximation by a great magnitude.

This approximation algorithm has incorporated a complete dynamic model that sometimes captures small but still contributing fluid forces. These forces are typically not incorporated into a sphere anemometer's algebraic deflection-wind speed model. The effects of the inline fluid terms can be expected to have a much more significant effect in a fluid with high density like water. Several possibilities as discussed in the previous chapter are available to continue pursuing results.

A Full-Bridge Wheatstone implementation would statistically reduce the strain measurement error and thus provide an increased accuracy in the wind approximations. Implementing a different restriction for the averaging time window due memory constraints could also affect the delay of the results and/or the accuracy to capture higher frequency wind model changes by the steady strain model.

Lastly the steady strain model has been dynamically modeled to incorporate the loads affecting sphere anemometer other than the drag of the mass sphere. By incorporating D'Alembert's Principle, Lagrange's Method, Euler-Bernoulli Beams, Navier-Stokes theory, and Young's Modulus the relationship to wind progressed into complete differential equations of motion.

REFERENCES

[1] B. Pedersen, T. Pedersen, H. Klung, N. Van Der Borg, N. Kelley, J. Dahlberg, Wind speed measurement and use of cup anemometry. In: Hunter, R.S. (Ed.), Expert Group Study on Recommended Particles for Wind Turbine Testing and Evaluation, vol. 11, second ed. International Energy Agency, 2003.

[2] M. Holling, B. Schulte, S. Barth, and J. Peinke, "Sphere Anemometer- A Faster Alternative Solution to Cup Anemometry," *Journal of Physics: Conference Series* vol. 75 no. 1, pp 1-6, 2007.

[3] R. Blevins, *Flow-Induced Vibrations*. New York, New York: Van Nostrand Reinhold, 1990, chapter 2.1-2.2, 6.1.

[4] J. Hurtado, *Kinematic and Kinetic Principles*. College Station, Texas: Lulu Marketplace, 2007.

[5] S. Han, H. Benaroya, and T. Wei, "Dynamics of Transversely Vibrating Beams Using Four Engineering Theories," *Journal of Sound and Vibrations*, Vol. 225, no. 5, pp. 935 – 988, 1999.

[6] C. L. Byrne, "Selected Topics in Applied Mathematics" in *Lecture Notes: University of Massachusetts Lowell*, 2011, pp. 257-262, http://faculty.uml.edu/cbyrne/amread.pdf

[7] National Instruments, *Strain Gauge Measurement*, Application Note 078, Austin, Texas, National Instruments Corporation, 1998.

[8] Agilent Technologies, *Practical Strain Gauge Measurements,* Application Note 290, Santa Clara, California, Agilent Technologies, 1999.

VITA

Name:	Davis Matthew Castillo
Address:	Department of Aerospace Engineering H.R. Bright Building, Ross Street-TAMU 3141 College Station, TX 77843-3141
Email Address:	calslider@gmail.com
Education:	B.S., Electrical Engineering, Southern Methodist University, 2007 B.S., Mathematics, Southern Methodist University, 2007 M.S., Aerospace Engineering, Texas A&M University, 2011